

JGR Solid Earth

RESEARCH ARTICLE

10.1029/2023JB026667

Key Points:

- The Moho and mantle transition zone (MTZ) discontinuities beneath Alaska are imaged by stacking long-period teleseismic SH waves
- Observed crustal thickness is generally consistent with surface topography and gravity measurements
- Our results suggest that the Pacific slab may have penetrated into the upper MTZ under central Alaska but not under the Alaska Peninsula

Supporting Information:

Supporting Information may be found in the online version of this article.

Correspondence to:

S. Hao,
s2hao@ucsd.edu

Citation:

Hao, S., Shearer, P., & Liu, T. (2023). The upper-mantle structure beneath Alaska imaged by teleseismic S-wave reverberations. *Journal of Geophysical Research: Solid Earth*, 128, e2023JB026667. <https://doi.org/10.1029/2023JB026667>

Received 5 MAR 2023

Accepted 16 MAY 2023

Author Contributions:

Conceptualization: Shangqin Hao, Peter Shearer
Data curation: Shangqin Hao
Formal analysis: Shangqin Hao
Funding acquisition: Peter Shearer
Investigation: Shangqin Hao
Methodology: Shangqin Hao, Peter Shearer, Tianze Liu
Project Administration: Peter Shearer
Resources: Peter Shearer, Tianze Liu
Software: Shangqin Hao, Peter Shearer
Supervision: Peter Shearer
Validation: Shangqin Hao
Visualization: Shangqin Hao
Writing – original draft: Shangqin Hao

© 2023. The Authors.

This is an open access article under the terms of the Creative Commons Attribution License, which permits use, distribution and reproduction in any medium, provided the original work is properly cited.

The Upper-Mantle Structure Beneath Alaska Imaged by Teleseismic S-Wave Reverberations

Shangqin Hao¹ , Peter Shearer¹ , and Tianze Liu¹ 

¹Institute of Geophysics and Planetary Physics, Scripps Institution of Oceanography, University of California, San Diego, La Jolla, CA, USA

Abstract Alaska is a tectonically active region with a long history of subduction and terrane accretion, but knowledge of its deep seismic structure is limited by a relatively sparse station distribution. By combining data from the EarthScope Transportable Array and other regional seismic networks, we obtain a high-resolution state-wide map of the Moho and upper-mantle discontinuities beneath Alaska using teleseismic SH-wave reverberations. Crustal thickness is generally correlated with elevation and the deepest Moho is in the region with basal accretion of the subducted Yakutat plate, consistent with its higher density due to a more mafic composition. The crustal thickness in the Brooks Range agrees with the prediction based on Airy isostasy and the weak free-air gravity anomaly, suggesting that this region probably does not have significant density anomalies. We also resolve the 410, 520, and 660 discontinuities in most regions, with a thickened mantle transition zone (MTZ) and a normal depth difference between the 520 and 660 discontinuities (d660-d520) under central Alaska, indicating the presence of the subducted Pacific slab in the upper MTZ. A near-normal MTZ and a significantly smaller d660-d520 are resolved under southeastern Alaska, suggesting potential mantle upwelling in the lower MTZ. Beneath the Alaska Peninsula, the thinned MTZ implies that the Pacific slab may not have reached the MTZ in this region, which is also consistent with recent tomography models. Overall, the results demonstrate a bent or segmented Pacific slab with varying depths under central Alaska and the Alaska Peninsula.

Plain Language Summary Alaska attracts attention from the Earth science community due to its complicated tectonic setting, including active subduction, crustal deformation, and extensive magmatism, but its deep structure remains enigmatic due to limited observations. With newly deployed dense Transportable-Array seismic stations across Alaska, we study Alaska's deep structure using a new imaging method. We find that the crust is thick beneath the northern and southern mountains and thin in the central flatlands, with a correlation between crustal thickness and elevation. The thickest crust lies in the region with basal accretion of the subducted Yakutat slab, an oceanic plateau with higher density than the normal continental crust. We also image the 410, 520, and 660 discontinuities beneath Alaska. Combining prior results with our findings, the subducted slab may have varying depths along strike, with the section beneath central Alaska penetrating into the upper mantle transition zone (MTZ) and the section beneath the Alaska Peninsula remaining above the MTZ.

1. Introduction

Located on the North American Plate and bounded by the Pacific Plate and the Arctic Ocean (Figure 1a), Alaska has a long history of subduction and terrane accretion (Plafker & Berg, 1994; Rioux et al., 2010; Trop et al., 2007), combined with active crustal deformation and magmatism (Brueckner et al., 2019; Finzel et al., 2015; Jadamec et al., 2013; Mazzotti & Hyndman, 2002; Moll-Stalcup et al., 1994; Plafker & Berg, 1994). At shallow depths, the Pacific plate subducts beneath Alaska at a rate of 5.7 cm/yr to the northwest (DeMets et al., 1990), and the plate boundary shifts from normal to shallow subduction and then to a transform fault, the Queen Charlotte-Fairweather Fault, from west to east (Plafker & Berg, 1994) (Figure 1a). This transition is correlated with the increasingly thickened Yakutat microplate, which is located beneath south-central Alaska and thought to be an oceanic plateau (G. L. Christeson et al., 2010; Chuang et al., 2017; Eberhart-Phillips et al., 2006; Elliott et al., 2013; Ferris et al., 2003; Gulick et al., 2007; Marechal et al., 2015), and its flat subduction may account for some unusual features in this region, such as the Denali volcanic gap and the Wrangell volcanism (Figure 1a) (G. L. Christeson et al., 2010; Eberhart-Phillips et al., 2006; Ward, 2015; Zhang et al., 2019).

Writing – review & editing: Shangqin Hao, Peter Shearer, Tianze Liu

There have been many studies of the crustal structure in Alaska, especially the crustal thickness and the V_p/V_s ratio in south-central Alaska, where the distinct Yakutat microplate is located. Veenstra et al. (2006) applied P receiver-function (PRF) analysis and found a sharp increase in crustal thickness across the Hines Creek fault from the northern lowland (26 km) to the Alaska Range (35–45 km) and a corresponding 4.6% increase in average crustal density required to explain the deviations from the crustal thickness predicted assuming simple Airy isostasy. Fuis et al. (2008) conducted the Trans-Alaska Crustal Transect investigation and observed the deepest Moho near the Pacific and Arctic margins (55 and 50 km, respectively), whereas the crustal thickness in central Alaska is only about 32 km. G. L. Christeson et al. (2010) and G. Christeson et al. (2013) focused on the crustal thickness in southern Alaska, especially its correlation with the Yakutat terrane. From south-southwest to north-northeast, the crustal thickness increases from 11.5 km for the Pacific Ocean crust to about 30 km for the Yakutat oceanic plateau crust across the Transition Fault and to 40–45 km beneath the Chugach-St. Elias Mountains. These results consistently show a positive correlation between crustal thickness and surface topography, but most of them deviate from the prediction assuming Airy isostasy and a homogeneous crustal density in southeastern Alaska. The discrepancy is often attributed to the distinctive composition and density of the Yakutat microplate. Eberhart-Phillips et al. (2006) found that the subducted Yakutat slab has a thick crust with low V_p and high V_p/V_s ratio while also observing a significant change in crustal thickness across the Denali fault. The variations of crustal thickness and V_p/V_s ratio across the Hines Creek Fault/Denali Fault were explained by the change in crustal composition from felsic-to-intermediate in the north to more mafic in the south (Brennan et al., 2011).

Recently, with the dramatic improvement in station coverage offered by the Earthscope Transportable Array (TA), state-wide crustal structures in Alaska were imaged in PRF and S receiver-function (SRF) studies (Gama et al., 2022; Mann et al., 2022; Miller et al., 2018; Zhang et al., 2019). All these results showed a consistent crustal-thickness pattern, with the thickest crust found beneath the Brooks Range and the Alaska Range. Nonetheless, there is still some disagreement in the absolute Moho depth in the region of the subducted Yakutat plate. Similar to the results in Eberhart-Phillips et al. (2006), Zhang et al. (2019) also found a higher-than-average V_p/V_s ratio in south-central Alaska, providing further evidence for the mafic composition of the Yakutat oceanic crust.

Plate reconstruction models show that the Kula-Pacific plate has been subducting beneath the North American Plate since the Mesozoic (Engebretson et al., 1985; Madsen et al., 2006; Müller et al., 2016; Seton et al., 2012), but there is disagreement on the location of the subducted plate, especially whether or not it has entered or penetrated the mantle transition zone (MTZ). Many seismic tomographic studies have identified the deep Pacific slab as a northeast (NE)-southwest (SW)-striking high-velocity anomaly extending from central Alaska to the Alaska Peninsula, but they have not reached a consensus on its depth extent. Among S-wave tomography studies, with more high-quality TA data, Martin-Short et al. (2018) observed high- V_s anomalies down to 600-km depth in central Alaska and shallower depths in the southwest. In contrast, Jiang et al. (2018) suggested that the high- V_s anomalies only reached about 450-km depth in central Alaska, although their velocity anomalies are stronger than the Martin-Short et al. results. Among P-wave tomography studies, Qi et al. (2007) found high- V_p anomalies within the MTZ beneath western Alaska, with a gap separating the upper part of the anomaly, which was interpreted as the Pacific plate, and the lower part, which was suggested to be the remnants of the Kula Plate. Both Burdick et al. (2017) and Boyce et al. (2023) found that the NE-SW-striking high-velocity feature extends as deep as 600-km depth, but the feature in the latter study is more concentrated in southwestern Alaska in the lower MTZ, whereas Gou et al. (2019) observed that the anomalies weaken significantly beyond 500-km depth.

Because phase transitions of the olivine system depend on the temperature and composition in the MTZ, slabs have a large effect on the topography of the MTZ discontinuities, which can be used to infer slab geometry. Both Dahm et al. (2017) and Van Stiphout et al. (2019) applied PRF stacking and found a thickened MTZ and an uplifted 410-km discontinuity (hereinafter “410”) in central Alaska, suggesting that the slab has reached the MTZ. Van Stiphout et al. (2019) applied appropriate velocity corrections and found little topography on the 660-km discontinuity (hereinafter “660”), suggesting that the slab probably has not reached the lower mantle. The discrepancy in “410” and “660” topography between different PRF studies could be partly due to the 3D velocity corrections, which significantly affect the discontinuity depths (M. Liu et al., 2022) yet have considerable uncertainty given the aforementioned disagreement between different tomography models.

Although the deep structures beneath Alaska have been investigated by numerous studies, some questions remain open. First, the older studies used sparse or small-aperture networks and thus obtained relatively small-scale or low-resolution results. The recent deployment of TA stations in Alaska was completed in 2021, providing

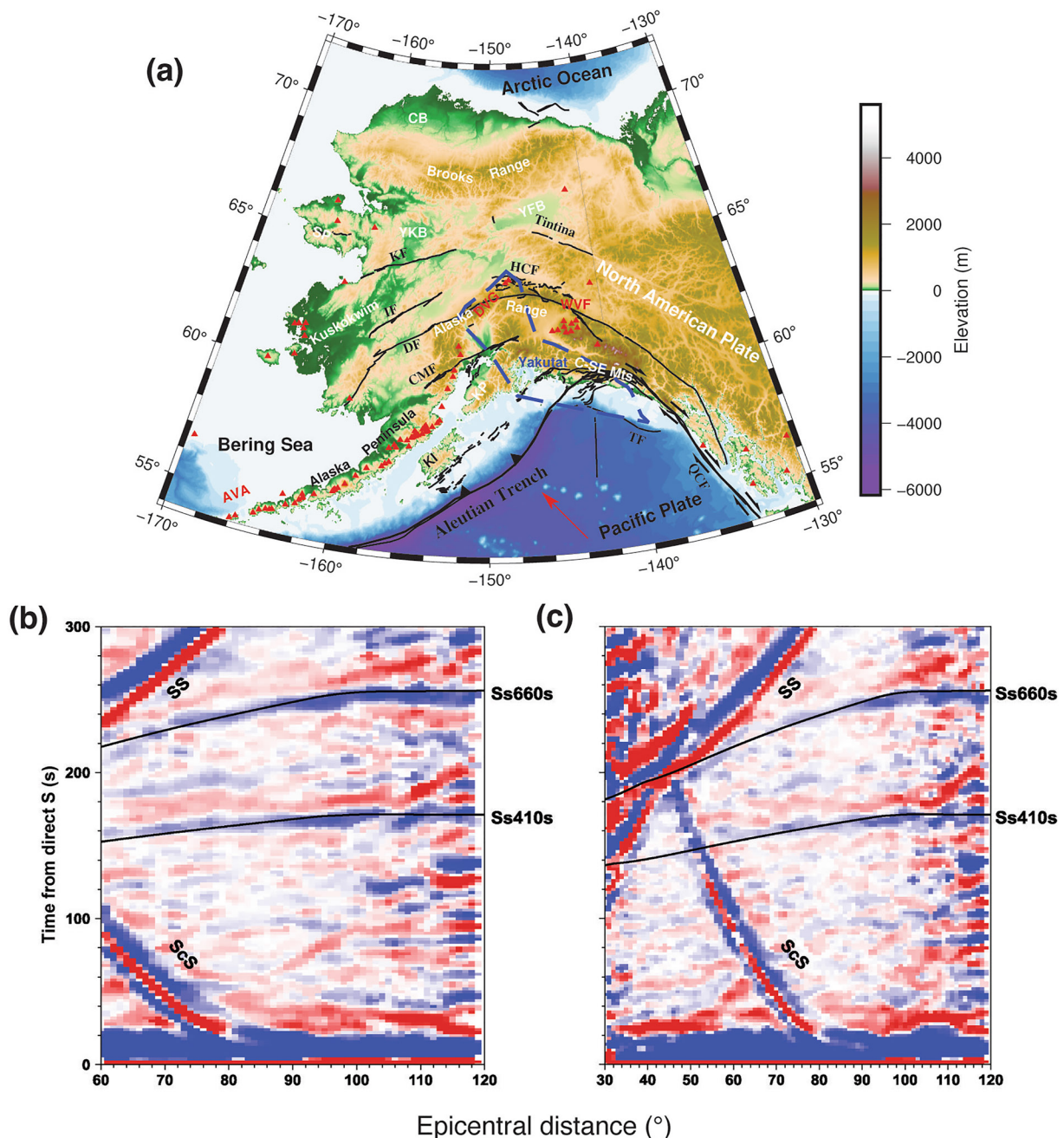


Figure 1. (a) Map of the research region. The Quaternary faults from the United States Geological Survey (<https://www.usgs.gov/natural-hazards/earthquake-hazards/faults>) are shown by black solid lines and the active volcanoes within the last 2 million years are shown as red triangles (Cameron, 2004) (<https://www.avo.alaska.edu/volcanoes/latlong.php>). Abbreviations of faults: CMF, Castle Mountain fault; DF, Denali Fault; HCF, Hines Creek Fault; IF, Iditarod-Nixon Fork fault; KF, Kaltag fault; Tintina, Tintina fault; TF, Transition fault; QCF, Queen Charlotte-Fairweather Fault; Abbreviations of other tectonic features: AVA, Aleutian volcanic arc; CB, Colville basin; C-SE Mts, Chugach-St. Elias Mountains; DVG, Denali volcanic gap; KI, Kodiak Island; KP, Kenai Peninsula; SP, Seward Peninsula; WVF, Wrangell volcanic field; Yakutat, Yakutat microplate; YFB, Yukon Flats basin; YKB, Yukon-Koyukuk basin. (b) and (c) are record section stacks of high-quality traces for the 10 and 5-s lowpass data sets, respectively, aligned and normalized on direct S, with the black curves denoting the predicted topside S-reflections at 410- and 660-km depths based on the iasp91 model (Kennett & Engdahl, 1991).

improved data coverage and thus an opportunity to obtain state-wide higher-resolution results. In addition, although PRFs and SRFs are widely used in imaging mantle discontinuities, PRFs are often obscured by sediment and crustal reverberations, and SRFs have poor depth resolution due to their low-frequency content and small temporal separations between conversions (T. Liu & Shearer, 2021). Shearer and Buehler (2019) developed

an inversion method for imaging station-side discontinuities using topside S reverberations, which are less affected by crustal multiples than PRFs and have better depth resolution than SRFs. Following this study, T. Liu and Shearer (2021) imaged shallow mantle structures under the contiguous US by analyzing only deep earthquakes to avoid contamination from source-side structures. In this study, we apply the S-reverberation method in Shearer and Buehler (2019) to the data collected by the local networks and all TA stations in Alaska to obtain high-resolution images of crustal and MTZ structures beneath the region.

2. Methods

2.1. Data Set and Processing

We obtain waveform data for 7,363 shallow earthquakes ($M_w > 5.5$, depth < 50 km, $30^\circ <$ epicentral distance $< 120^\circ$) recorded by TA and other regional networks (7C, AK, AT, AV, CN, II, IM, IU, US, XE, XN, XR, XZ YE, YM, and YV) from January 2000 to September 2021, which covers the entire time period of the TA deployment in Alaska. Because we use SH waves for our analysis, we rotate the horizontal components to radial and transverse directions and retain only the transverse components. Following some experimentation, we found that 5-s and 10-s lowpass filters are the highest frequencies that produce stable and similar results to those obtained using lower-frequency filters for the crust and MTZ, respectively. Taking both stability and resolution into account, we thus generate images for the crust and MTZ using the 5-s and 10-s data sets, respectively. After filtering the data, we downsample the records to 1 Hz and align and normalize them to the maximum amplitude of direct S (Shearer, 1991). To select data with good signal-to-noise ratios and clean S-wave arrivals, we define three windows similar to those in T. Liu and Shearer (2021), which are the source window (25 s before and after direct S), the noise window (25–50 s before direct S), and the coda window (25–250 s after direct S), and retain traces satisfying the following criteria:

1. The ratio between the mean absolute amplitude in the source window and the noise window is larger than 5;
2. The ratio between the mean absolute amplitude in the source window and the coda window is larger than 1;
3. The ratio between the maximum absolute amplitude in the source window and coda window is larger than 1;
4. The ratio between the maximum absolute amplitude and mean absolute amplitude in the source window is larger than 3;
5. Each event needs to be recorded by at least 10 stations.

These criteria successfully reject traces with strong noise, coda, or extended source-time functions.

Next, we stack and normalize the traces in 1° increments in epicentral distance and 2-s increments in time with direct S as the reference phase, flipping the polarity when direct S has negative amplitude (Figures 1b and 1c). These record sections exhibit clear topside reflections $Ss410s$ and $Ss660s$ and are similar to Figure 1 in Shearer and Buehler (2019). Since there are strong SS and ScS arrivals interfering with the MTZ discontinuity phases at distances less than 60° , we only use traces between 60° and 120° for the 10-s data set. For the shallow structure, we use the data from 30° to 120° but exclude data points within 20 s of ScS for our subsequent analysis. After pre-processing, 41,998 seismograms from 1,065 events and 35,278 seismograms from 752 events remain for the 10-s (Figure 1b) and 5-s data sets (Figure 1c), respectively.

We trace the topside reflection rays using the 1D iasp91 model (Kennett & Engdahl, 1991) to determine their reflection points for assumed horizontal discontinuities at depths from 350 to 800 km in 5-km increments for the 10-s data set and from 5 to 71 km in 2-km increments for the 5-s data set. Since the time-to-depth conversion is affected by 3D shear-velocity structure (M. Liu et al., 2022), we correct the $Ssds$ -S differential times using 3D velocity models. At each reflected depth, we assume the 1D ray path, compute the average velocity deviation with respect to the iasp91 model along the two-way reverberation path of $Ssds$ on the receiver side, and then calculate the deviation of differential time. We use two recent S-wave tomography models of Alaska from Martin-Short et al. (2018) (hereinafter MS18 model) and Jiang et al. (2018) (hereinafter J18 model) for the MTZ and the CRUST1.0 model (Laske et al., 2013) for the crust. We then define a model in 120° – 180° W and 50° – 75° N and divide it into $4^\circ \times 2^\circ$ cells with 2° and 1° overlaps in the W-E and N-S directions, respectively. Note that these cells have equal N-S and E-W dimensions at 60° N and thus are approximately square across most of Alaska. Next we apply the common-reflection-point method and obtain the sum of receiver-side reflections within each cell by minimizing both source and receiver terms using an iterative least-square inversion approach (Shearer & Buehler, 2019). Finally, considering the credibility and resolution of the results (see Section 2.2 for more detail),

we smooth the results horizontally using a radially symmetric \cos^2 taper with a 3° radius and treat only the grid cells contributed by more than 100 bounce points as robust.

For topside reflection imaging of the crust, we can avoid the leakage of source-side structure into the image by using earthquakes deeper than the Moho (T. Liu & Shearer, 2021). Therefore, we checked our results by separately processing earthquakes deeper than 60 km (Figure S1 in Supporting Information S1). The spatial coverage of the image, based on the same criteria (a minimum of 100 bounce points), is limited due to the scarcity of deep earthquakes. However, the main features of the Moho are consistent between the results produced using shallow and deep events. Therefore, we will only discuss the results obtained using shallow earthquakes in our subsequent analysis.

2.2. Synthetic Tests

It should be noted that a fundamental trade-off exists between source-side and receiver-side terms in our inversion and our least squares (L2-norm) minimization method cannot completely eliminate the leakage of source-side reflectors into the receiver-side terms, which could generate spurious receiver-side reflectors. Because our results are produced using sources in many different regions, this leakage is most likely to occur for global discontinuities, such as the “410” and “660.” Nonetheless, receiver-side topography of these reflectors should still be resolvable given sufficient data coverage. On the other hand, receiver-side reflectors that are only present beneath some of the stations may generate spurious reflections under the other stations, with the polarity and amplitude of the artifacts depending upon the presence or absence of a corresponding source-side reflector and the fraction of the receivers containing the reflection. These issues are discussed in more detail in Shearer and Buehler (2019).

In order to assess the robustness of our method based on our specific data sets, we conduct a series of synthetic tests with varying source-side and receiver-side structures. Our approach consists of the following steps:

1. On the source side, we divide the Earth into equal-area latitude-longitude cells with a cell spacing r and randomly assign depths of the “410” and “660” with Gaussian distributions of $\mathcal{N}(410, \sigma_{410}^2)$ and $\mathcal{N}(660, \sigma_{660}^2)$ (unit: km), respectively. The 520-km discontinuity (hereinafter “520”) is assumed to exist at exactly 520-km depth in half of the cells chosen randomly.
2. On the receiver side, we divide the study area into latitude-longitude cells with spacings of $2a$ in longitude and a in latitude. A checkerboard model is assumed, with the “410” depth alternating between 400 and 420 km, the “660” depth alternating between 640 and 680 km, and the “520” present at a depth of 520 km in half of the cells with a checkerboard pattern (Figures 2a–2c).
3. The receiver-side amplitude contribution to the results is set to 1, with the source-side contribution represented by *src_amp*.
4. For each trace in the final data set, we calculate the arrival times of reflected phases on both source and receiver sides according to event and station locations and discontinuity settings utilizing the iasp91 model (Kennett & Engdahl, 1991). Then we generate vertical lines (stick seismograms) at these times with the amplitude equal to the product of the topside reflection coefficients and the sum of source- and receiver-side contributions. The reflection coefficients off the “410” and “660” are calculated based on the iasp91 model (Kennett & Engdahl, 1991) and the impedance contrast of the “520” is assumed to be 2.9% (Shearer, 1996).
5. The synthetic data set is then created by convolving the stick seismograms with the direct S phase (± 15 s around direct S) for each trace.
6. Finally, the synthetic data set is processed in the same manner as the observed data set.

We initially evaluate the impact of source-side structures on the results by examining different combinations of source-side parameters, with a fixed at a large value of 5° . Tests 1–3 (Figures 2d–2f) show the results with decreasing variations of the “410” and “660” depths (σ_{410} and σ_{660}), which indicate a minor influence of the standard deviations of the source-side discontinuity depths. In Test 2, the smaller σ_{410} and σ_{660} cause slightly diminished receiver-side discontinuity amplitudes compared to Test 1 without affecting the discontinuity depths. Test 3 shows a weak leakage from the source side without any depth variations. Since the scenario in Test 3 is highly unrealistic (constant 410 and 660 depths below all sources), we set σ_{410} and σ_{660} to the relatively small values in Test 2 (5 km) for the subsequent tests. The cell spacing on the source side, r , also has a negligible impact on the results (Figure S2 in Supporting Information S1) and thus we set r to a small value of 3° for the following tests.

We find that a significantly larger source-side contribution can compromise the ability to resolve receiver-side structures (Test 2 vs. Test 4 in Figure 2). However, such a large source-side contribution is unlikely because

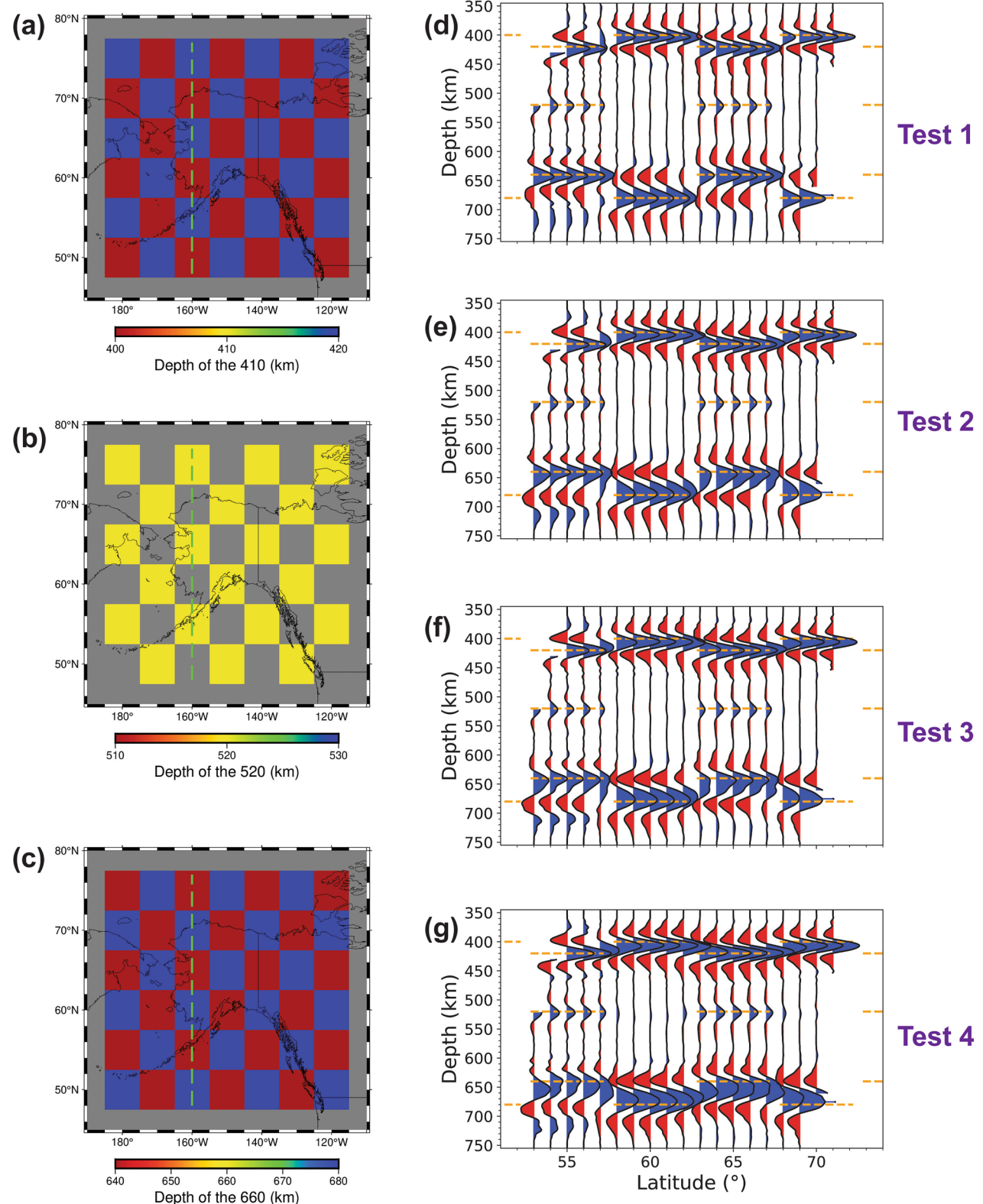


Figure 2. Synthetic test results. (a–c) The assumed receiver-side depths of the “410,” “520,” and “660” with checkerboard patterns, respectively. (d–g) The cross-sections along 160°W (green dashed lines in (a–c)) of four tests based on varying source-side parameters. The horizontal orange dashed lines represent the assumed discontinuity depths in (a–c). Fixed parameters: $a = 5^\circ$, $r = 3^\circ$. Other parameters: (d) Test 1: $src_amp = 1$, $\sigma_{410} = 20$ km, $\sigma_{660} = 30$ km; (e) Test 2: $src_amp = 1$, $\sigma_{410} = \sigma_{660} = 5$ km; (f) Test 3: $src_amp = 1$, $\sigma_{410} = \sigma_{660} = 0$ km; (g) Test 4: $src_amp = 2$, $\sigma_{410} = \sigma_{660} = 5$ km. See text for details.

we stack and average results from different source regions. As we reject events with less than 10 stations and only plot grid cells contributed by 100 seismograms, we expect src_amp to be close to one, that is, there is no reason to expect source-side reflectors to be any brighter than receiver-side reflectors on average. In this case, the source-side structure has an insignificant impact on the final results for the checkerboard model with $a = 5^\circ$. Furthermore, using a set of reasonable and stringent source-side parameters ($r = 3^\circ$, $\sigma_{410} = \sigma_{660} = 5$ km, and $src_amp = 1$), we assess the capability of source- and receiver-side separation for varying scales of the checkerboard model. The results in Figure S3 in Supporting Information S1 indicate that the structures larger than approximately 3° in the checkerboard model can be resolved. We note that this synthetic test is only a measure of our ability to separate source- and receiver-side structure, not the true resolution of our imaging approach. Based on the Fresnel-zone sizes at MTZ depths given by Shearer and Buehler (2019) and the resolution tests performed by M. Liu et al. (2022), we smooth the results using a radially symmetric \cos^2 taper with a 3° radius and treat only structures with scales greater than 3° as reliably resolved.

3. Results

The N-S cross-sections of our reflection images for the crust and the MTZ are shown in Figures 3 and 4, respectively, and the distribution of corresponding events and stations are shown in Figures 3f and 4j. We define positive- and negative-polarity reflectors as impedance increases and decreases with depth and color them blue and red, respectively. Standard errors are estimated using bootstrap resampling (randomly sampling the seismograms with replacement), which are denoted by the thin dashed lines surrounding the traces. The number of seismograms contributing to the data stack of each grid cell is shown in Figures 3e and 4i. The data density is significantly higher in south-central Alaska mainly because many non-TA stations with long operation times are concentrated in this region (Figures 3f and 4j). To focus on the most reliable results, we do not plot grid cells with less than 100 seismograms and shade only the reflectors with absolute amplitudes larger than one standard error in blue or red. These cross-sections show clear S-reflections off the Moho and MTZ discontinuities in most regions (Figures 3 and 4). In general, the reflectors in central and northern Alaska are more continuous and consistent than those in southern Alaska, which may be due to the complicated tectonic setting near the Pacific margin.

3.1. Crust

The Moho discontinuity is resolved with significant amplitude in most cross-sections and is notably shallower in central Alaska than in the north and south, consistent with the surface elevation (Figure 3). Our results reveal a single prominent peak at depths greater than 20 km in most cross-sections, along with other noteworthy features. In the west (cross-sections A1 and A2 in Figure 3), there is a series of strong negative pulses at a depth of approximately 30 km near the Alaska Peninsula, which diminish gradually north of 60°N , near the Denali volcanic gap. In the east (cross-sections A3 and A4 in Figure 3), there are double positive peaks at depths of approximately 20 and 50 km, respectively, in the range of $59^\circ\text{--}62^\circ\text{N}$.

The negative pulses observed in the southwestern region are subparallel to the Aleutian volcanic arc and the low-velocity zone at the depth of 28 km imaged by various previous tomography studies (Martin-Short et al., 2018; Ward & Lin, 2018; Yang & Gao, 2020). This low-velocity zone also disappears at approximately 60°N , suggesting that the negative pulses may represent a low-velocity layer within the crust. The double peaks in the east coincide with the Yakutat microplate (Figure 3e) and are at depths similar to the upper interface of the Yakutat plate and the Yakutat Moho imaged by Mann et al. (2022). The thin low-velocity layer imaged by Mann et al. (2022) is absent in our results likely because of the lower frequency of our data. Assuming the two peaks represent the top and bottom of the Yakutat crust, we can estimate its thickness by measuring the depth difference between the two peaks, which gives a crustal thickness of 25–30 km (Figure S4 in Supporting Information S1). The crustal thickness increases slightly from west to east, consistent with the trend in Mann et al. (2022), although our values are significantly larger in the west. These results support the theory that Yakutat plate is an oceanic plateau actively colliding with the North America plate (G. L. Christeson et al., 2010; Chuang et al., 2017; Eberhart-Phillips et al., 2006; Elliott et al., 2013; Ferris et al., 2003; Gulick et al., 2007; Marechal et al., 2015).

We define a positive peak as the Moho if (a) it is the strongest in the depth range of 25–60 km, (b) it has an amplitude greater than 2% of the direct S amplitude, and (c) the peak is contributed by more than 100 traces. The resulting Moho topography, shown in Figure 5a, ranges from 26 to 56 km, with an average crustal thickness

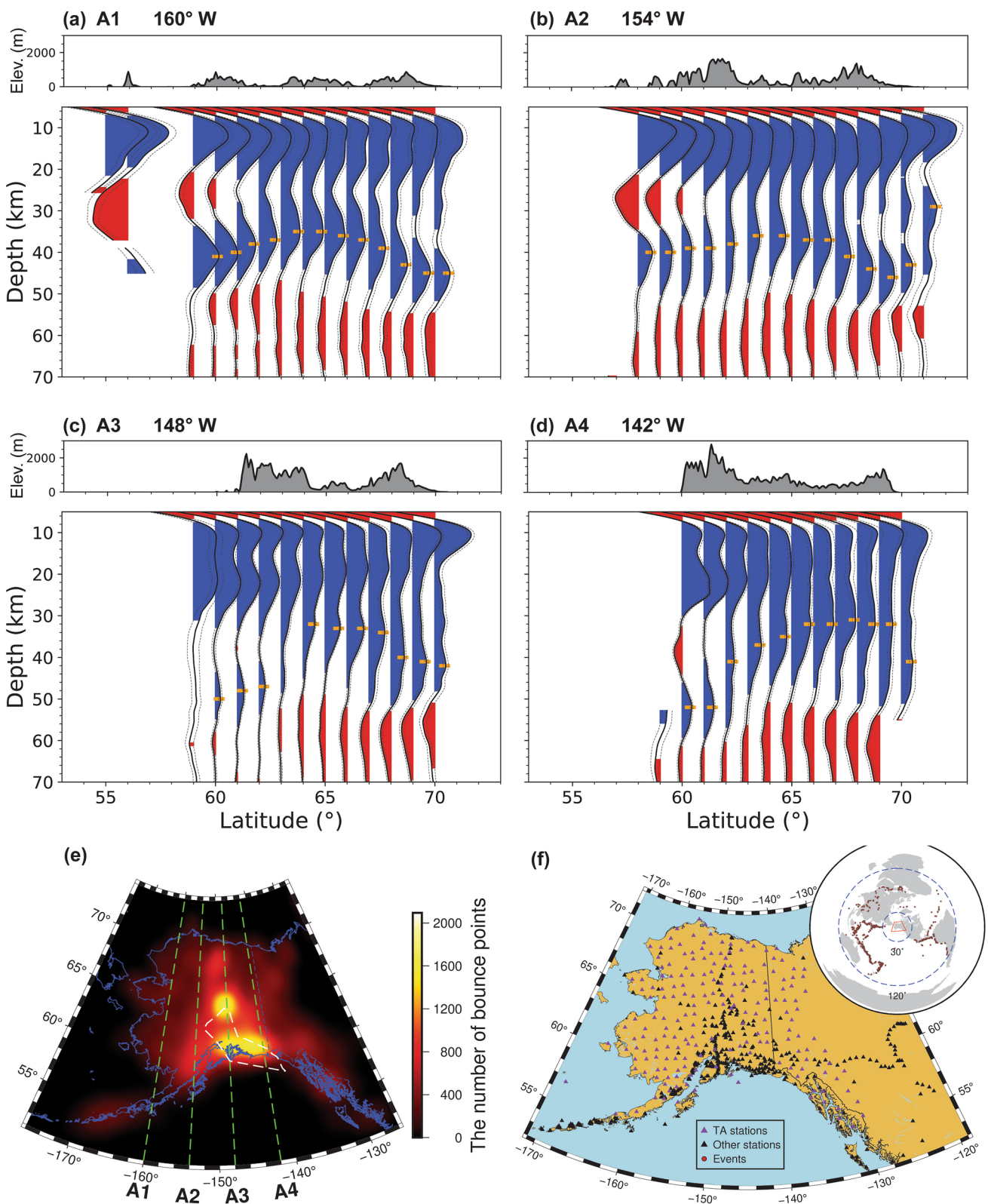


Figure 3.

of 39 km. The deepest Moho is located in the Yakutat microplate region (45–50 km). The topography shows a shallow Moho beneath the central lowlands and a deep Moho beneath the northern and southern mountain ranges, exhibiting a positive correlation between crustal thickness and elevation.

The correlation between Moho depth and surface topography agrees with prior results (Gama et al., 2022; Mann et al., 2022; Miller et al., 2018; Zhang et al., 2019) but there is a discrepancy in the absolute Moho depth, particularly in the region where the Yakutat slab subducts. In this region, Gama et al. (2022) and Mann et al. (2022) found similar crustal thickness to our results, which is greater than the previous PRF results (around 40 km) (Miller et al., 2018; Zhang et al., 2019). The difference between our results and Zhang et al. (2019) is illustrated in Figure 5d, which may be partly due to the lower depth resolution of our results in southeastern Alaska. The Moho arrival in this region is broad (Figures 3c and 3d), making it difficult to determine the Moho depth precisely. However, the upper bound of our Moho depth in the region is still deeper than 45 km, suggesting other explanations for the discrepancy, particularly the velocity models used for converting from depth to time. For example, although Zhang et al. (2019) used multiple phases in the $H - \kappa$ method to constrain the average crustal V_p/V_s ratio, uncertainties still arise from the assumed crustal V_p and the trade-off between Moho depth and V_p/V_s ratio. Specifically, an overestimated V_p/V_s can cause an underestimation of Moho depth for a given average crustal V_p (Zhang et al., 2019).

Assuming the study region is in isostatic equilibrium, the Moho depth (d_{moho}) can be calculated using the surface elevation (h), a reference crustal thickness ($d_0 = 35$ km), and assumed crustal and mantle density ($\rho_c = 2,800 \text{ kg/m}^3$ and $\rho_m = 3,300 \text{ kg/m}^3$, respectively) through the equation $d_{moho} = d_0 + \frac{\rho_m}{\rho_m - \rho_c} h$. The difference between the Moho depth estimated from our seismic image and the isostatic prediction is shown in Figure 5c. Although the absolute depth difference depends on the assumed reference Moho depth and density contrast across the Moho, the relative difference still reveals possible density anomalies in the crust and uppermost mantle. Compared with the isostatic prediction, the most notable features are the deeper seismic Moho in the region of subducted Yakutat crust and the shallower seismic Moho in northeastern and east-central Alaska. The observed high free-air gravity anomaly (Chen et al., 2022) (Figure S5 in Supporting Information S1) in the region of subducted Yakutat plate suggests the presence of high-density anomalies at shallow depths. This anomaly probably resides primarily in the Yakutat crust, which was interpreted to be more mafic and thus denser than normal continental crust due to the origin of the Yakutat microplate as an oceanic plateau (G. L. Christeson et al., 2010). In contrast, the seismic Moho is shallower than the isostatic prediction in northeastern and east-central Alaska, probably due to a lower average crustal density or a higher uppermost-mantle density than assumed in our calculation. However, the crustal thickness difference from the isostatic prediction is insignificant in the Brooks Range. The minor difference is consistent with the weak free-air gravity anomaly in the Brooks Range (Chen et al., 2022) (Figure S5 in Supporting Information S1), suggesting that this region is not likely to have significant density anomalies.

3.2. MTZ Discontinuities

In the MTZ depth range of our image, the “410” and “660” are clearly resolved in most cross-sections and the “520” is also widely present with relatively weak amplitude (Figure 4). At latitudes higher than 60°N, the peaks near 410- and 660-km depths have large amplitudes and are relatively clean. The “520” shows comparable amplitudes to the “410” in the west (cross-sections A1 and A2 in Figure 4) and becomes weaker in the east (cross-sections A3 and A4 in Figure 4), which is consistent with the large-scale decreasing S520S/S410S amplitude ratio from west to east in Alaska (Tian et al., 2020) and could result from varying impedance contrasts and sharpness of the discontinuity or other factors. At latitudes lower than 60°N, the peaks are complex and sometimes consist of multiple peaks with similar amplitudes in some regions, particularly in the results based on the MS18 model, making it difficult to determine reliable discontinuity depths. In cross-sections A1 and A2, the results based on the J18 model exhibit more consistent “410” and “660” peaks than those based on the MS18

Figure 3. N-S (a–d) topography and cross-sections at depths shallower than 70 km corrected using the CRUST 1.0 model (Laske et al., 2013). Positive- and negative-polarity reflectors represent impedance increases and decreases with depth and are shown in blue and red, respectively. The ± 1 standard error is represented by dashed lines surrounding the data stack and only the grid points with absolute amplitudes larger than one standard error are shaded. The Moho picks are marked as orange bars and the corresponding topography variations are plotted in Figure 5. The locations of the cross-sections and the number of bounce points for each cell at 35-km depth are shown in (e), with the white dashed line representing the contour of the Yakutat microplate (Eberhart-Phillips et al., 2006). The distribution of stations and events for the 5-s filtered seismograms is shown in (f). The triangles represent the seismic stations with TA shown in purple and the other stations in black. The inset shows the distribution of events, denoted by red dots, with the red enclosed area representing the research region.

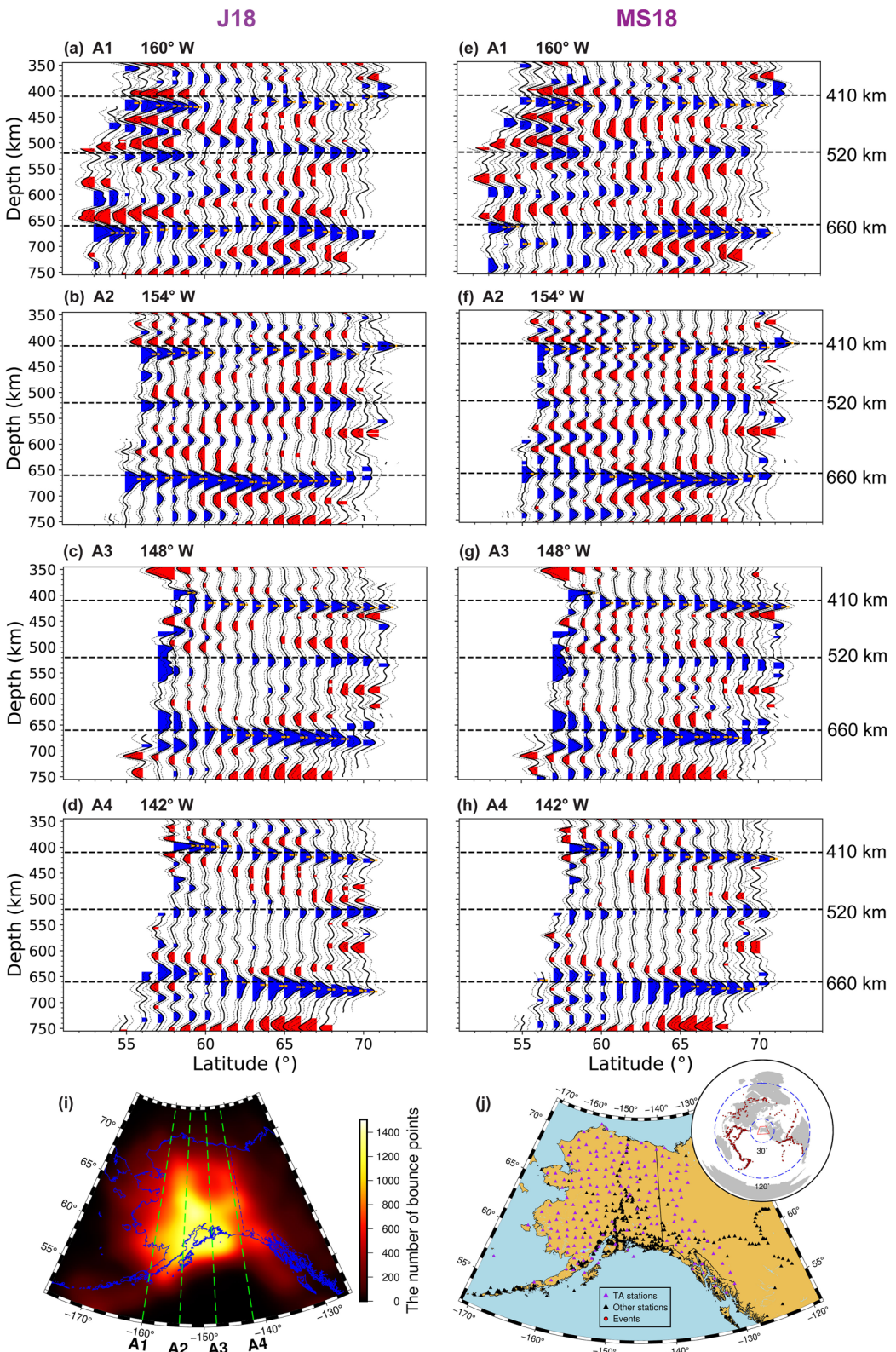


Figure 4. N-S cross-sections in the MTZ across Alaska as corrected for the J18 (a–d) and MS18 (e–h) 3D velocity models. The color and dashed lines in (a–h) are consistent with Figure 3 and the horizontal black dashed lines represent depths of 410, 520, and 660 km. The “410” and “660” picks are marked as orange bars and the corresponding topography variations are plotted in Figure 6. The locations of the cross-sections and the number of bounce points for each cell at 535-km depth are shown in (i). The distribution of stations and events for the 10-s filtered seismograms is shown in (j) and symbols have the same definition as in Figure 3f.

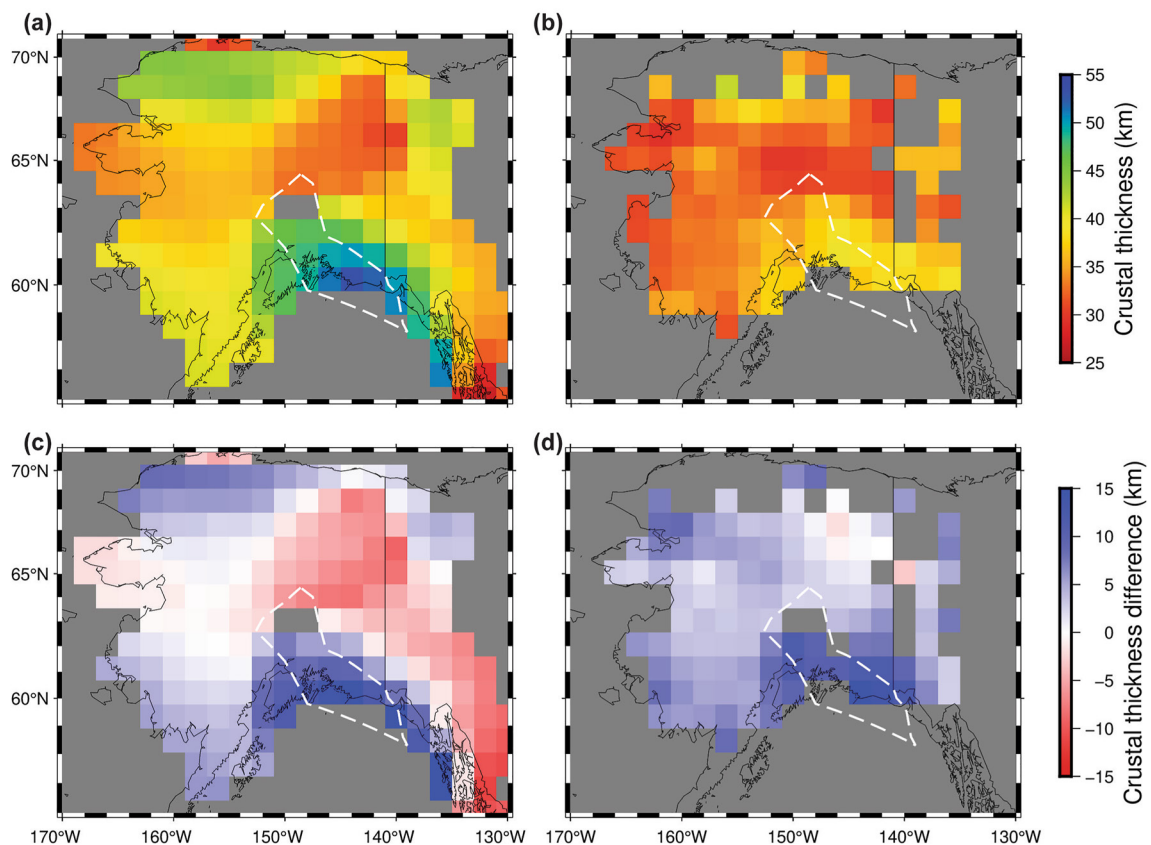


Figure 5. Comparison of Moho depths. (a) Our Moho depth results corrected using the CRUST1.0 model (Laske et al., 2013). Only the results with a peak amplitude greater than 2% of the direct S amplitude and contributed by over 100 bounce points are plotted. (b) Moho depth results from Zhang et al. (2019). (c) Difference between our results and the isostatic prediction based on a reference crustal thickness of 35 km. (d) Difference between our results and the results from Zhang et al. (2019). In (c) and (d), positive values indicate that our results are greater than the comparison results. The white dashed line denotes the contour of the Yakutat slab (Eberhart-Phillips et al., 2006).

model. However, in cross-sections A3 and A4, both results exhibit complex “660” arrivals south of 60°N, complicating the estimation of “660” depth in southeastern Alaska.

In southwestern Alaska (cross-section A1 in Figure 4), both results show a series of strong peaks between the “410” and “520” at a depth of about 480 km. We determine that these features are not caused by contamination from source-side structures because the adjacent regions, which are also sampled by the sources from the same region (mostly the Fiji-Tonga subduction zone), do not show these features. In addition, both results show prominent peaks at a depth of approximately 600 km in the 55°–65°N range in the west (cross-sections A1 and A2), which do not appear in the east (cross-sections A3 and A4). However, as this feature has a lower amplitude compared to the “410” and “660” and comparable amplitude to adjacent negative pulses, the possibility of it being an artifact cannot be ruled out. Moreover, both models consistently exhibit strong negative pulses below the “660” in west-central Alaska (near 65°N in cross-sections A1 and A2), which are absent in cross-sections A3 and A4.

We estimate the depths of the “410” and “660” by searching for the strongest peak in the range of 390–450 and 630–710 km, respectively. To focus on the most reliable features, we require that the candidate peak exceeds 1% of the direct S amplitude and the number of bounce points exceeds 100. Since the impedance contrast of the “520” is only about 30% of the “410” (Tian et al., 2020), we estimate the “520” depth where its amplitude is at least 0.3% within the depth range of 490–540 km. To reduce ambiguities caused by multiple peaks with comparable amplitudes that satisfy the amplitude criteria, we further require that the highest peak should be at least 2 times stronger than the second highest peak. We will hereinafter refer to these as “robust” observations of “410,” “520,” and “660” depths, which are shown in Figures 6 and 7, respectively.

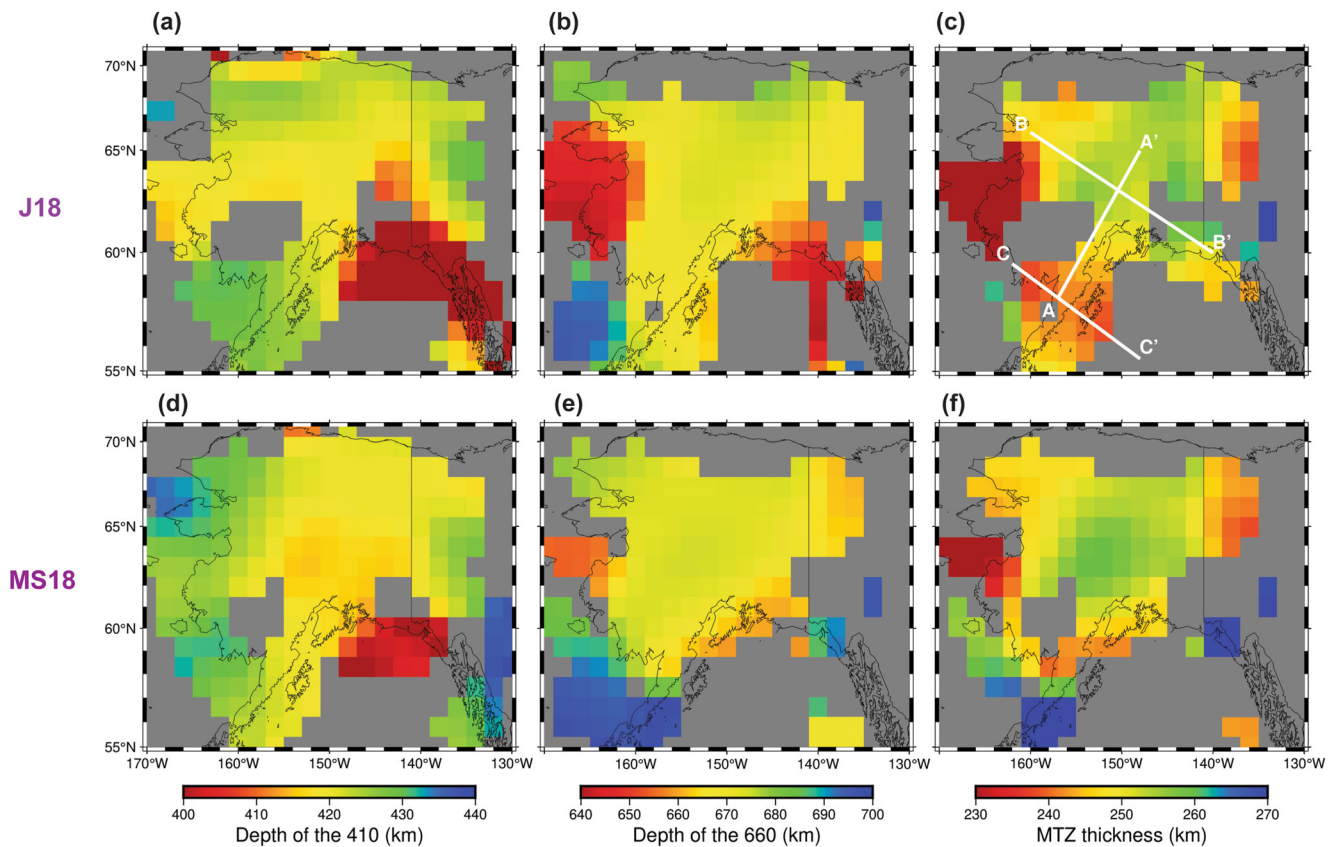


Figure 6. Estimated “410” and “660” depths and the MTZ thickness corrected using the J18 (a–c) and MS18 (d–f) 3D velocity models. Only results with a peak amplitude of at least 1% of the direct S amplitude, at least twice as strong as the second-highest peak, and contributed by more than 100 bounce points are plotted. The locations of the cross sections in Figure S6 in Supporting Information S1 are shown in (c).

Due to different coverage of the “410” and “660” bounce points and deviations caused by 3D velocity variations, we mainly focus on the areas with both robust “410” and “660.” The average depths of the “410” and “660” are 418 and 668 km for the results produced using the J18 model, with standard deviations of 10 and 14 km, respectively, and the average MTZ thickness in regions with both robust “410” and “660” observations is 248 ± 12 km. In contrast, the corresponding values in the results produced using the MS18 model are 422 ± 8 , 674 ± 11 , and 251 ± 12 km, respectively. These MTZ thickness results are larger than the global average of 242 km (e.g., Y. Gu et al., 1998; Lawrence & Shearer, 2006) and are likely caused by the deep slab subducted to the MTZ. Since the majority of the “410” and “660” depths lie within the range of 390–440 and 640–700 km, respectively, we use these ranges for plotting in Figure 6 instead of the searching range. There is no significant variation in the “520” topography except the deeper “520” in southeastern Alaska and the shallower “520” in Kuskokwim (Figure 7). The average depths of the “520” are 520 and 521 km for the J18 and MS18 models, respectively.

Although the absolute depths of MTZ discontinuities estimated using the two velocity models are different in some regions, the depth variation and depth differences between discontinuities are mostly consistent between the two results. Both results show elevated “410” and slightly depressed “660” in central Alaska, corresponding to a thickened MTZ of about 260 km. The two results also consistently show thinned MTZ under the Seward Peninsula and Kuskokwim (Figures 6c and 6f). However, due to the ambiguous “660” peaks at low latitudes (Figure 4), the MTZ depths estimated using the MS18 model show significant lateral changes in the southeastern and southwestern regions (Figure 6f). In contrast, the results using the J18 model are more continuous in these regions, showing significantly thinned MTZ under the Alaska Peninsula and normal MTZ under Chugach-St. Elias Mountains (Figure 6c).

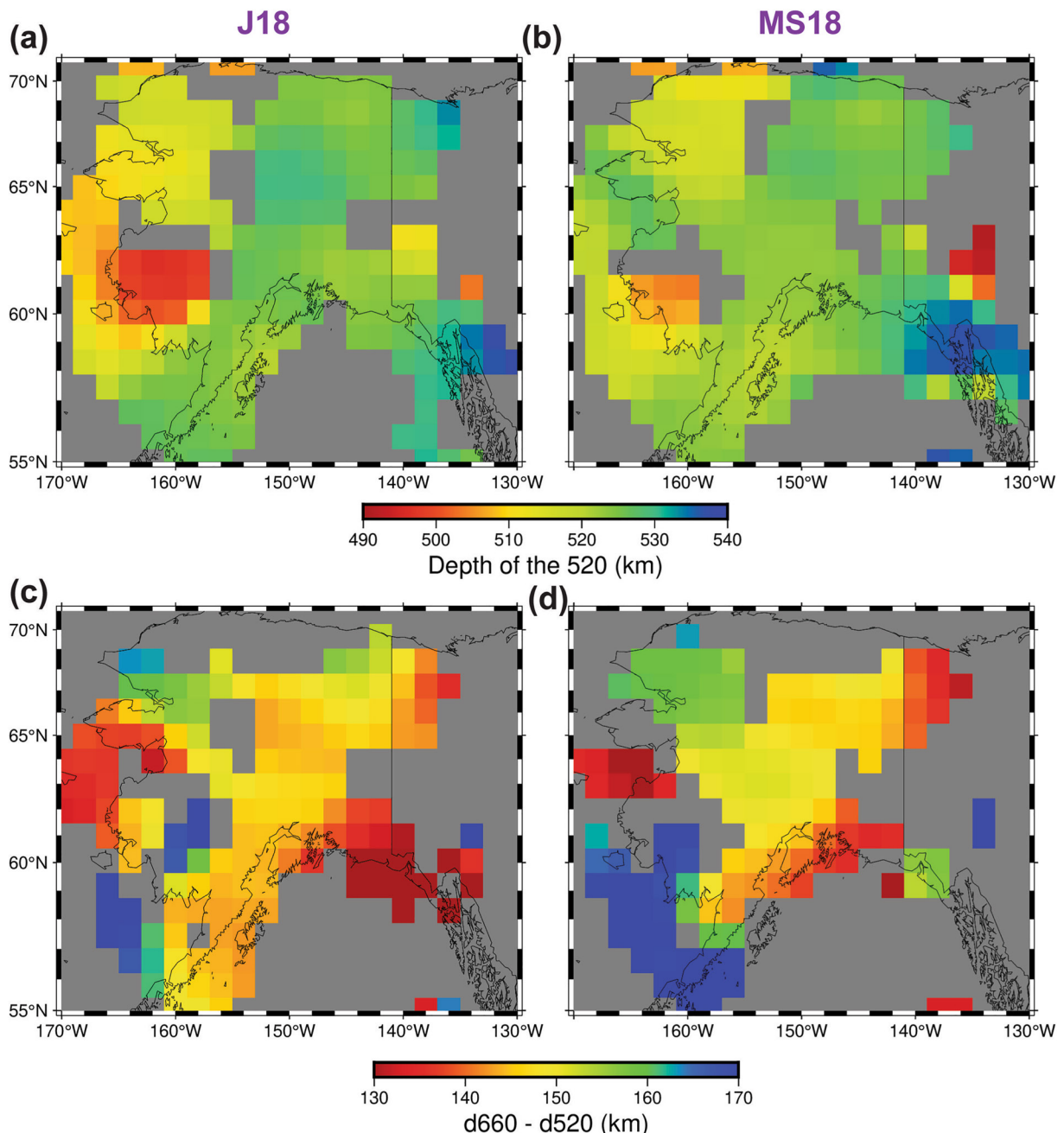


Figure 7. Estimated “520” depths (a–b) and the depth difference between the “660” and the “520” (c–d) using the J18 (the left column) and MS18 (the right column) 3D velocity models. Only “520” results with a peak amplitude of at least 0.3% of the direct S amplitude, at least twice as strong as the second-highest peak, and contributed by more than 100 bounce points are plotted in (a) and (b).

4. Discussion

4.1. Effect of 3D Velocity Models

The absolute depths of MTZ discontinuities resolved with our method depend strongly on the chosen 3D upper shear-velocity structures (M. Liu et al., 2022). The MS18 and J18 models used in this study show a high-velocity NE-SW-striking slab from central Alaska to the Alaska Peninsula, which extends from the lithosphere to at least 300-km depth and is surrounded by low-velocity anomalies. Therefore, the corrected discontinuity depths are expected to increase in the high-velocity region and decrease in the surrounding regions compared with

the 1D results. However, the tomography models can be inaccurate and thus cause under- or over-correction of discontinuity depths. For instance, in cross-sections A3 and A4 (Figure 4), the “410” and “660” depths show a strong positive correlation, and the “410” is considerably shallow in southeastern Alaska, where both P and S wave tomography models reveal a notable low-velocity anomaly (Burdick et al., 2017; Gou et al., 2019; Jiang et al., 2018; Martin-Short et al., 2018; Qi et al., 2007), suggesting the existence of the Northern Cordilleran slab window and mantle upwelling through this window (Gou et al., 2019; Madsen et al., 2006; Qi et al., 2007; Van Stiphout et al., 2019). This upwelling is expected to depress the “410” based on mineral physics models (Katsura & Ito, 1989), inconsistent with the elevated “410” shown in our results. We thus speculate that the depths of both “410” and “660” may be over-corrected to shallower depths in this region.

The corrections based on tomography models also have a significant impact on the amplitude and stacking coherence of the MTZ discontinuities, particularly in southwestern and southeastern Alaska/northwestern Canada in this study. Compared with the results corrected using the MS18 model, the correction based on the J18 model improves the stacking coherence and thereby increases the amplitude of the discontinuities and reduces the number of ambiguous double peaks at low latitudes (Figure 4). The more coherent stacking leads to shallower “660” and thinner MTZ in the southeastern region, which is more consistent with the low-velocity anomalies in the MTZ shown by the tomography models. In summary, the choice of tomography model has a considerable effect on the estimated amplitude, coherence, and depth of the discontinuities. To better understand the effects of 3D velocity structures and resolve more accurate discontinuities, it may be useful to jointly invert for discontinuity perturbations and velocity structures using different data types and constraints (e.g., Y. J. Gu et al., 2003).

4.2. Comparison With Previous Studies and Implications for Slab Geometry

PRFs are commonly used to image mantle discontinuities and are primarily sensitive to the S-velocity contrasts across discontinuities, whereas our approach is sensitive to the contrasts in impedance, the product of V_s and density. Because both methods are used to resolve discontinuity structures below seismic receivers, combining both types of observations may lead to better understanding of the nature of the discontinuities. Recent PRF results from Dahm et al. (2017) and Van Stiphout et al. (2019), as well as our study, use similar Alaska tomography models (Martin-Short et al., 2016, 2018), facilitating comparisons. All results show elevated “410,” slightly depressed “660,” and thus thick MTZ in central Alaska (near 64°N, 150°W in Figure 6), suggesting that the Pacific slab has entered the MTZ in this region. This is consistent with recent tomography models (e.g., Boyce et al., 2023; Gou et al., 2019; Jiang et al., 2018; Martin-Short et al., 2018). Furthermore, the results of applying the appropriate corrections based on the MS18 and J18 models exhibit little topography on the “660” (Van Stiphout et al., 2019) in central Alaska, indicating that the slab has probably not penetrated into the lower mantle. In addition to the MTZ thickness, the depth difference between the “520” and “660” (hereinafter d660-d520) can be utilized to interpret the thermal state in the MTZ, particularly the lower MTZ. The Clapeyron slope of the wadsleyite-ringwoodite phase transition (6.91 MPa/K from Suzuki et al. (2000); 4.11 MPa/K from Inoue et al. (2006)) is larger than that of the olivine-wadsleyite transition (4.0 MPa/K from Katsura et al. (2004)), so d660-d520 is more sensitive to the temperature variation. Recent experimental studies suggest that the depths of the wadsleyite-ringwoodite phase transition and the post-spinel transition are 500–514 km (Tsujino et al., 2019) and 660 km (Chanyshov et al., 2022) along a normal mantle adiabat, respectively, corresponding to a d660-d520 of 146–160 km. Our results show that d660-d520 is slightly less than 150 km in central Alaska (Figure 7), which implies a normal or higher-than-normal temperature. Combining the MTZ thickness with d660-d520 results, the subducted Pacific slab under central Alaska has probably only reached the upper MTZ. Another significant feature in prior results is the thinned MTZ and the low-velocity anomaly in the MTZ beneath southeastern Alaska/northwestern Canada, but our result shows a near-normal MTZ thickness (Figure 6c) and a significantly smaller d660-d520 in this region (Figure 7c), which probably indicates a higher-than-normal temperature in the lower MTZ instead of the whole MTZ.

Both PRF and our results exhibit a consistently thinned MTZ in western Alaska, under the Seward Peninsula and Kuskokwim, although this feature is less prominent in Van Stiphout et al. (2019). This region is situated below the volcanoes and is underlain by a vertical low-velocity column extending to the MTZ in recent S-wave tomography models (Jiang et al., 2018; Martin-Short et al., 2018). Such a feature is also consistent with a small d660-d520 in this region (Figure 7), possibly indicating hot mantle upwelling from a relatively great depth. Between Kuskokwim and the subducted slab in central Alaska, the mantle wedge shows weaker “410” amplitudes (cross-section

A1 in Figure 4) than other regions, with some even falling below our 1% amplitude criterion for identifying the “410.” This area corresponds to the “410” gap near 61°N, 160°W in Figures 6a and 6d, consistent with the observations from Van Stiphout et al. (2019) as well. This feature is likely caused by the high water content in the MTZ released by the slab (e.g., Chen et al., 2002; Frost & Dolejš, 2007).

Our results confirmed the pronounced thickening of the MTZ in central Alaska shown by previous studies, suggesting the presence of the subducted Pacific slab in the MTZ beneath the region. However, the MTZ gradually becomes thinner toward the southwest (Figures 6c and 6f), suggesting an increase in MTZ temperature (Katsura & Ito, 1989). Recent P and S wave tomography models (Gou et al., 2019; Jiang et al., 2018; Martin-Short et al., 2018) show a steeply subducting slab in this region, but the main high-velocity anomaly does not extend beyond 410-km depth in most studies, significantly shallower than in central Alaska (Figure S6 in Supporting Information S1). The latest P-wave model (Boyce et al., 2023) revealed that the high-velocity anomalies from central to southwestern Alaska are broadly continuous above 400-km depth but become less continuous in the MTZ below the Alaska Peninsula and the Aleutian volcanic arc, where weak low-velocity anomalies are imaged at 400-km depth. Given the thin MTZ and the depth extent of the high-velocity anomalies, the slab is unlikely to have entered the MTZ beneath southwestern Alaska. Instead, the thin MTZ could be caused by upwelling of hot material from greater depths. The presence of a low-velocity anomaly below the high-velocity slab, as observed in some tomography models (Boyce et al., 2023; Gou et al., 2019; Jiang et al., 2018), provides evidence for this interpretation, although further investigations are needed to confirm this hypothesis. By combining multiple types of observations, we conclude that the NE-SW-striking Pacific slab is likely bent or segmented, with the northeastern section beneath central Alaska having entered the upper MTZ but not the lower MTZ and the southwestern section beneath the Alaska Peninsula not yet reaching the MTZ.

5. Conclusions

Using data from the recently completed TA and other regional networks, we obtain a map of upper-mantle discontinuities across Alaska using teleseismic SH-wave reverberations. The Moho and MTZ discontinuities are resolved in most regions with amplitudes well above uncertainty estimates. The Moho is generally shallow in the central lowlands and deep in the northern and southern mountainous regions, consistent with isostatic predictions. The anomalously deep Moho in southeastern Alaska may result from the more mafic and thus denser crust of the Yakutat microplate.

Our results show a thickened MTZ and a normal d660-d520 in central Alaska likely caused by the presence of the subducted slab in the upper MTZ. We also find a normal MTZ and a small d660-d520 in southeastern Alaska likely caused by hot mantle upwelling in the lower MTZ. Below the Alaska Peninsula, the thinned MTZ and the depth extent of high-velocity anomalies revealed by previous tomography studies suggest that the slab has not reached the MTZ yet. Therefore, the subducted Pacific slab beneath Alaska is likely bent or segmented, with its northeastern part inside the upper MTZ and its southwestern part above the MTZ.

Data Availability Statement

Our data were obtained from IRIS Data Management Center (<https://ds.iris.edu/ds/nodes/dmc/>) funded by the National Science Foundation, under Cooperative Agreement EAR-1851048. Files with robust depths of the Moho, 410-km, and 660-km discontinuities are available in Tables S1–S7 and the Zenodo database (<https://doi.org/10.5281/zenodo.7893924>).

References

- Boyce, A., Liddell, M., Pugh, S., Brown, J., McMurchie, E., Parsons, A., et al. (2023). A new P-wave tomographic model (CAP22) for North America: Implications for the subduction and cratonic metasomatic modification history of western Canada and Alaska. *Journal of Geophysical Research: Solid Earth*, 128(3), e2022JB025745. <https://doi.org/10.1029/2022jb025745>
- Brennan, P. R., Gilbert, H., & Ridgway, K. D. (2011). Crustal structure across the central Alaska Range: Anatomy of a Mesozoic collisional zone. *Geochemistry, Geophysics, Geosystems*, 12(4). <https://doi.org/10.1029/2011gc003519>
- Brueseke, M. E., Benowitz, J. A., Trop, J. M., Davis, K. N., Berkelhammer, S. E., Layer, P. W., & Morter, B. K. (2019). The Alaska Wrangell Arc: ~30 Ma of subduction-related magmatism along a still active arc-transform junction. *Terra Nova*, 31(1), 59–66. <https://doi.org/10.1111/ter.12369>
- Burdick, S., Vernon, F. L., Martynov, V., Eakins, J., Cox, T., Tytell, J., et al. (2017). Model update May 2016: Upper-mantle heterogeneity beneath North America from travel-time tomography with global and USAArray data. *Seismological Research Letters*, 88(2A), 319–325. <https://doi.org/10.1785/0220160186>

Acknowledgments

Funding for this work was provided by the National Science Foundation (Grants EAR-1620251, EAR-1829601, and EAR-2123529). We would like to express our sincere gratitude to the following individuals for providing valuable data that greatly contributed to this study: Dr. Robert Martin-Short from Berkeley Seismological Laboratory, University of California, Berkeley, who provided their tomography model; Dr. Aibing Li from the Department of Earth and Atmospheric Sciences, University of Houston, who provided their crustal thickness results. We are grateful for the invaluable feedback, suggestions, and constructive criticism from the editor and reviewers, which have greatly helped us to improve the quality of our work.

- Cameron, C. (2004). The geologic database of information on volcanoes in Alaska (GeoDIVA): A comprehensive and authoritative source for volcanic information. *Alaska GeoSurvey News*, 7(1), 1–2.
- Chanyshhev, A., Ishii, T., Bondar, D., Bhat, S., Kim, E. J., Farla, R., et al. (2022). Depressed 660-km discontinuity caused by akimotoite–bridgemanite transition. *Nature*, 601(7891), 69–73. <https://doi.org/10.1038/s41586-021-04157-z>
- Chen, J., Inoue, T., Yurimoto, H., & Weidner, D. J. (2002). Effect of water on olivine-wadsleyite phase boundary in the $(\text{Mg}, \text{Fe})_2\text{SiO}_4$ system. *Geophysical Research Letters*, 29(18), 22–1–22–4. <https://doi.org/10.1029/2001gl014429>
- Chen, J., Zhang, X., Chen, Q., Shen, Y., & Nie, Y. (2022). Static gravity field recovery and accuracy analysis based on reprocessed GOCE level 1b gravity gradient observations. In *EGU general assembly conference abstracts* (pp. EGU22–6771).
- Christeson, G., Van Avendonk, H., Gulick, S., Reece, R., Pavlis, G., & Pavlis, T. (2013). Moho interface beneath Yakutat terrane, southern Alaska. *Journal of Geophysical Research: Solid Earth*, 118(9), 5084–5097. <https://doi.org/10.1002/jgrb.50361>
- Christeson, G. L., Gulick, S. P., van Avendonk, H. J., Worthington, L. L., Reece, R. S., & Pavlis, T. L. (2010). The Yakutat terrane: Dramatic change in crustal thickness across the Transition fault, Alaska. *Geology*, 38(10), 895–898. <https://doi.org/10.1130/g31170.1>
- Chuang, L., Bostock, M., Wech, A., & Plourde, A. (2017). Plateau subduction, intraslab seismicity, and the Denali (Alaska) volcanic gap. *Geology*, 45(7), 647–650. <https://doi.org/10.1130/g38867.1>
- Dahm, H. H., Gao, S. S., Kong, F., & Liu, K. H. (2017). Topography of the mantle transition zone discontinuities beneath Alaska and its geodynamic implications: Constraints from receiver function stacking. *Journal of Geophysical Research: Solid Earth*, 122(12), 10–352. <https://doi.org/10.1002/2017jb014604>
- DeMets, C., Gordon, R. G., Argus, D., & Stein, S. (1990). Current plate motions. *Geophysical Journal International*, 101(2), 425–478. <https://doi.org/10.1111/j.1365-246x.1990.tb06579.x>
- Eberhart-Phillips, D., Christensen, D. H., Brocher, T. M., Hansen, R., Ruppert, N. A., Haeussler, P. J., et al. (2006). Imaging the transition from Aleutian subduction to Yakutat collision in central Alaska, with local earthquakes and active source data. *Journal of Geophysical Research*, 111(B11). <https://doi.org/10.1029/2005jb004240>
- Elliott, J., Freymueller, J. T., & Larsen, C. F. (2013). Active tectonics of the St. Elias orogen, Alaska, observed with GPS measurements. *Journal of Geophysical Research: Solid Earth*, 118(10), 5625–5642. <https://doi.org/10.1002/jgrb.50341>
- Engbeartson, D. C., Cox, A., & Gordon, R. G. (1985). Relative motions between oceanic and continental plates in the Pacific basin.
- Ferris, A., Abers, G. A., Christensen, D. H., & Veenstra, E. (2003). High resolution image of the subducted Pacific (?) plate beneath central Alaska, 50–150 km depth. *Earth and Planetary Science Letters*, 214(3–4), 575–588. [https://doi.org/10.1016/s0012-821x\(03\)00403-5](https://doi.org/10.1016/s0012-821x(03)00403-5)
- Finzel, E. S., Flesch, L. M., Ridgway, K. D., Holt, W. E., & Ghosh, A. (2015). Surface motions and intraplate continental deformation in Alaska driven by mantle flow. *Geophysical Research Letters*, 42(11), 4350–4358. <https://doi.org/10.1002/2015gl063987>
- Frost, D. J., & Dolejš, D. (2007). Experimental determination of the effect of H_2O on the 410-km seismic discontinuity. *Earth and Planetary Science Letters*, 256(1–2), 182–195. <https://doi.org/10.1016/j.epsl.2007.01.023>
- Fuis, G. S., Moore, T. E., Plafker, G., Brocher, T. M., Fisher, M. A., Mooney, W. D., et al. (2008). Trans-Alaska Crustal Transect and continental evolution involving subduction underplating and synchronous foreland thrusting. *Geology*, 36(3), 267–270. <https://doi.org/10.1130/g24257a.1>
- Gama, I., Fischer, K. M., & Hua, J. (2022). Mapping the lithosphere and asthenosphere beneath Alaska with Sp converted waves. *Geochemistry, Geophysics, Geosystems*, 23(10), e2022GC010517. <https://doi.org/10.1029/2022gc010517>
- Gou, T., Zhao, D., Huang, Z., & Wang, L. (2019). Aseismic deep slab and mantle flow beneath Alaska: Insight from anisotropic tomography. *Journal of Geophysical Research: Solid Earth*, 124(2), 1700–1724. <https://doi.org/10.1029/2018jb016639>
- Gu, Y., Dziewonski, A. M., & Agee, C. B. (1998). Global de-correlation of the topography of transition zone discontinuities. *Earth and Planetary Science Letters*, 157(1–2), 57–67. [https://doi.org/10.1016/s0012-821x\(98\)00027-2](https://doi.org/10.1016/s0012-821x(98)00027-2)
- Gu, Y. J., Dziewoński, A. M., & Ekström, G. (2003). Simultaneous inversion for mantle shear velocity and topography of transition zone discontinuities. *Geophysical Journal International*, 154(2), 559–583. <https://doi.org/10.1046/j.1365-246x.2003.01967.x>
- Gulick, S. P., Lowe, L. A., Pavlis, T. L., Gardner, J. V., & Mayer, L. A. (2007). Geophysical insights into the Transition fault debate: Propagating strike slip in response to stalled Yakutat block subduction in the Gulf of Alaska. *Geology*, 35(8), 763–766. <https://doi.org/10.1130/g23585a.1>
- Inoue, T., Irfune, T., Higo, Y., Sanehira, T., Sueda, Y., Yamada, A., et al. (2006). The phase boundary between wadsleyite and ringwoodite in Mg_2SiO_4 determined by in situ X-ray diffraction. *Physics and Chemistry of Minerals*, 33, 106–114. <https://doi.org/10.1007/s00269-005-0053-y>
- Jadamec, M. A., Billen, M. I., & Roeske, S. M. (2013). Three-dimensional numerical models of flat slab subduction and the Denali fault driving deformation in south-central Alaska. *Earth and Planetary Science Letters*, 376, 29–42. <https://doi.org/10.1016/j.epsl.2013.06.009>
- Jiang, C., Schmandt, B., Ward, K. M., Lin, F.-C., & Worthington, L. L. (2018). Upper mantle seismic structure of Alaska from Rayleigh and S wave tomography. *Geophysical Research Letters*, 45(19), 10–350. <https://doi.org/10.1029/2018gl079406>
- Katsura, T., & Ito, E. (1989). The system $\text{Mg}_2\text{SiO}_4\text{-Fe}_2\text{SiO}_4$ at high pressures and temperatures: Precise determination of stabilities of olivine, modified spinel, and spinel. *Journal of Geophysical Research*, 94(B11), 15663–15670. <https://doi.org/10.1029/jb094ib11p15663>
- Katsura, T., Yamada, H., Nishikawa, O., Song, M., Kubo, A., Shinmei, T., et al. (2004). Olivine-wadsleyite transition in the system $(\text{Mg}, \text{Fe})_2\text{SiO}_4$. *Journal of Geophysical Research*, 109(B2). <https://doi.org/10.1029/2003jb002438>
- Kennett, B., & Engdahl, E. (1991). Traveltimes for global earthquake location and phase identification. *Geophysical Journal International*, 105(2), 429–465. <https://doi.org/10.1111/j.1365-246x.1991.tb06724.x>
- Laske, G., Masters, G., Ma, Z., & Pasyanos, M. (2013). Update on CRUST1.0—A 1-degree global model of Earth's crust. *Geophysical Research Abstracts*, 15, 2658.
- Lawrence, J. F., & Shearer, P. M. (2006). A global study of transition zone thickness using receiver functions. *Journal of Geophysical Research*, 111(B6). <https://doi.org/10.1029/2005jb003973>
- Liu, M., Ritsema, J., & Chaves, C. A. (2022). Influence of shear-wave velocity heterogeneity on SH wave reverberation imaging of the mantle transition zone. *Geophysical Journal International*, 231(3), 2144–2155. <https://doi.org/10.1093/gji/gjac321>
- Liu, T., & Shearer, P. M. (2021). Complicated lithospheric structure beneath the contiguous US revealed by teleseismic S-reflections. *Journal of Geophysical Research: Solid Earth*, 126(5), e2020JB021624. <https://doi.org/10.1029/2020jb021624>
- Madsen, J., Thorkelson, D., Friedman, R. M., & Marshall, D. (2006). Cenozoic to Recent plate configurations in the Pacific Basin: Ridge subduction and slab window magmatism in western North America. *Geosphere*, 2(1), 11–34. <https://doi.org/10.1130/ges00020.1>
- Mann, M. E., Abers, G. A., Daly, K. A., & Christensen, D. H. (2022). Subduction of an oceanic plateau across southcentral Alaska: Scattered-wave imaging. *Journal of Geophysical Research: Solid Earth*, 127(1), e2021JB022697. <https://doi.org/10.1029/2021jb022697>
- Marchal, A., Mazzotti, S., Elliott, J. L., Freymueller, J. T., & Schmidt, M. (2015). Indentor-corner tectonics in the Yakutat-St. Elias collision constrained by GPS. *Journal of Geophysical Research: Solid Earth*, 120(5), 3897–3908. <https://doi.org/10.1002/2014jb011842>
- Martin-Shorth, R., Allen, R., Bastow, I. D., Porritt, R. W., & Miller, M. S. (2018). Seismic imaging of the Alaska subduction zone: Implications for slab geometry and volcanism. *Geochemistry, Geophysics, Geosystems*, 19(11), 4541–4560. <https://doi.org/10.1029/2018gc007962>

- Martin-Short, R., Allen, R. M., & Bastow, I. D. (2016). Subduction geometry beneath south central Alaska and its relationship to volcanism. *Geophysical Research Letters*, 43(18), 9509–9517. <https://doi.org/10.1002/2016gl070580>
- Mazzotti, S., & Hyndman, R. D. (2002). Yakutat collision and strain transfer across the northern Canadian Cordillera. *Geology*, 30(6), 495–498. [https://doi.org/10.1130/0091-7613\(2002\)030<0495:ycast>2.0.co;2](https://doi.org/10.1130/0091-7613(2002)030<0495:ycast>2.0.co;2)
- Miller, M. S., O'Driscoll, L. J., Porritt, R. W., & Roeske, S. M. (2018). Multiscale crustal architecture of Alaska inferred from P receiver functions. *Lithosphere*, 10(2), 267–278. <https://doi.org/10.1130/l1701.1>
- Moll-Stalcup, E. J., Plafker, G., & Berg, H. (1994). Latest Cretaceous and Cenozoic magmatism in mainland Alaska. *The Geology of Alaska*, 1, 589–619.
- Müller, R. D., Seton, M., Zahirovic, S., Williams, S. E., Matthews, K. J., Wright, N. M., et al. (2016). Ocean basin evolution and global-scale plate reorganization events since Pangea breakup. *Annual Review of Earth and Planetary Sciences*, 44(1), 107–138. <https://doi.org/10.1146/annurev-earth-060115-012211>
- Plafker, G., & Berg, H. C. (1994). Overview of the geology and tectonic evolution of Alaska.
- Qi, C., Zhao, D., & Chen, Y. (2007). Search for deep slab segments under Alaska. *Physics of the Earth and Planetary Interiors*, 165(1–2), 68–82. <https://doi.org/10.1016/j.pepi.2007.08.004>
- Rioux, M., Mattinson, J., Hacker, B., Kelemen, P., Blusztajn, J., Hanghøj, K., & Gehrels, G. (2010). Intermediate to felsic middle crust in the accreted Talkeetna arc, the Alaska Peninsula and Kodiak Island, Alaska: An analogue for low-velocity middle crust in modern arcs. *Tectonics*, 29(3). <https://doi.org/10.1029/2009tc002541>
- Seton, M., Müller, R. D., Zahirovic, S., Gaina, C., Torsvik, T., Shephard, G., et al. (2012). Global continental and ocean basin reconstructions since 200 Ma. *Earth-Science Reviews*, 113(3–4), 212–270. <https://doi.org/10.1016/j.earscirev.2012.03.002>
- Shearer, P. M. (1991). Constraints on upper mantle discontinuities from observations of long-period reflected and converted phases. *Journal of Geophysical Research*, 96(B11), 18147–18182. <https://doi.org/10.1029/91jb01592>
- Shearer, P. M. (1996). Transition zone velocity gradients and the 520-km discontinuity. *Journal of Geophysical Research*, 101(B2), 3053–3066. <https://doi.org/10.1029/95jb02812>
- Shearer, P. M., & Buehler, J. (2019). Imaging upper-mantle structure under USArray using long-period reflection seismology. *Journal of Geophysical Research: Solid Earth*, 124(9), 9638–9652. <https://doi.org/10.1029/2019jb017326>
- Suzuki, A., Ohtani, E., Morishima, H., Kubo, T., Kanbe, Y., Kondo, T., et al. (2000). In situ determination of the phase boundary between wadsleyite and ringwoodite in Mg_2SiO_4 . *Geophysical Research Letters*, 27(6), 803–806. <https://doi.org/10.1029/1999gl008425>
- Tian, D., Lv, M., Wei, S. S., Dorfman, S. M., & Shearer, P. M. (2020). Global variations of Earth's 520- and 560-km discontinuities. *Earth and Planetary Science Letters*, 552, 116600. <https://doi.org/10.1016/j.epsl.2020.116600>
- Trop, J. M., Ridgway, K. D., Glen, J., & O'Neill, J. (2007). Mesozoic and Cenozoic tectonic growth of southern Alaska: A sedimentary basin perspective. *Special Papers - Geological Society of America*, 431, 55.
- Tsujino, N., Yoshino, T., Yamazaki, D., Sakurai, M., Sun, W., Xu, F., et al. (2019). Phase transition of wadsleyite-ringwoodite in the $\text{Mg}_2\text{SiO}_4\text{-Fe}_2\text{SiO}_4$ system. *American Mineralogist*, 104(4), 588–594. <https://doi.org/10.2138/am-2019-6823>
- Van Stiphout, A., Cottaar, S., & Deuss, A. (2019). Receiver function mapping of mantle transition zone discontinuities beneath Alaska using scaled 3-D velocity corrections. *Geophysical Journal International*, 219(2), 1432–1446. <https://doi.org/10.1093/gji/ggz360>
- Veenstra, E., Christensen, D. H., Abers, G. A., & Ferris, A. (2006). Crustal thickness variation in south-central Alaska. *Geology*, 34(9), 781–784. <https://doi.org/10.1130/g22615.1>
- Ward, K. M. (2015). Ambient noise tomography across the southern Alaskan Cordillera. *Geophysical Research Letters*, 42(9), 3218–3227. <https://doi.org/10.1002/2015gl063613>
- Ward, K. M., & Lin, F.-C. (2018). Lithospheric structure across the Alaskan cordillera from the joint inversion of surface waves and receiver functions. *Journal of Geophysical Research: Solid Earth*, 123(10), 8780–8797. <https://doi.org/10.1029/2018jb015967>
- Yang, X., & Gao, H. (2020). Segmentation of the Aleutian-Alaska subduction zone revealed by full-wave ambient noise tomography: Implications for the along-strike variation of volcanism. *Journal of Geophysical Research: Solid Earth*, 125(11), e2020JB019677. <https://doi.org/10.1029/2020jb019677>
- Zhang, Y., Li, A., & Hu, H. (2019). Crustal structure in Alaska from receiver function analysis. *Geophysical Research Letters*, 46(3), 1284–1292. <https://doi.org/10.1029/2018gl081011>